Integrated Ultramicroelectrode–Nanopipet Probe for Concurrent Scanning Electrochemical Microscopy and Scanning Ion Conductance Microscopy

David J. Comstock,[†] Jeffrey W. Elam,[‡] Michael J. Pellin,[§,||] and Mark C. Hersam*,[†,||]

Department of Materials Science and Engineering, Northwestern University, Evanston, Illinois 60208, Energy Systems Division and Materials Science Division, Argonne National Laboratory, Argonne, Illinois 60439, and Department of Chemistry, Northwestern University, Evanston, Illinois 60208

Scanning ion conductance microscopy (SICM) has developed into a powerful tool for imaging a range of biophysical systems. In addition, SICM has been integrated with a range of other techniques, allowing for the simultaneous collection of complementary information including near-field optical and electrophysiological properties. However, SICM imaging remains insensitive to electrochemical properties, which play an important role in both biological and nonbiological systems. In this work, we demonstrate the fabrication and application of a nanopipet probe with an integrated ultramicroelectrode (UME) for concurrent SICM and scanning electrochemical microscopy (SECM). The fabrication process utilizes atomic layer deposition (ALD) of aluminum oxide to conformally insulate a gold-coated nanopipet and focused ion beam (FIB) milling to precisely expose a UME at the pipet tip. Fabricated probes are characterized by both scanning electron microscopy and cyclic voltammetry and exhibit a 100 nm diameter nanopipet tip and a UME with an effective radius of 294 nm. The probes exhibit positive and negative feedback responses on approach to conducting and insulating surfaces, respectively. The suitability of the probes for SECM–SICM imaging is demonstrated by both feedback-mode and substrate generation/tip collection-mode imaging on patterned surfaces. This probe geometry enables successful SECM–SICM imaging on features as small as 180 nm in size.

In recent years, scanning ion conductance microscopy (SICM)[1–3] has emerged as a versatile noncontact imaging tool. As such, SICM has been applied to numerous biophysical systems, including proteins in cell membranes,[4] suspended artificial membranes,[5] ionic conductivity of porous membranes,[6] and mechanical properties of living cells.[7] Additionally, SICM has been integrated with a range of complementary techniques, including confocal microscopy,[8] scanning near-field optical microscopy (SNOM),[9,10] and patch clamping.[11] These auxiliary measurements provide additional information about the sample that is correlated with the surface topography detected by SICM imaging. Despite these impressive advancements in SICM, it remains insensitive to electrochemical properties. Spatial mapping of electrochemistry is commonly achieved by scanning electrochemical microscopy (SECM) and has been widely used in the study of electrode surfaces,[12–14] membrane transport,[15–18] and biological systems.[19–21] In this work, we extend the capabilities of SICM to electrochemical

---

* To whom correspondence should be addressed. E-mail: m-hersam@northwestern.edu. Phone: 847-491-2696. Fax: 847-491-7820.
† Department of Materials Science and Engineering, Northwestern University.
‡ Energy Systems Division, Argonne National Laboratory.
§ Materials Science Division, Argonne National Laboratory.
|| Department of Chemistry, Northwestern University.

(1) Hansma, P. K.; Drake, B.; Marti, O.; Gould, S. A. C.; Prater, C. B. *Science* **1989**, *243*, 641–643.
(2) Korchev, Y. E.; Bashford, C. L.; Milovanovic, M.; Vodyanoy, I.; Lab, M. J. *Biophys. J.* **1997**, *73*, 653–658.
(3) Novak, P.; Li, C.; Shevchuk, A. I.; Stepanyan, R.; Caldwell, M.; Hughes, S.; Smart, T. G.; Gorelik, J.; Ostanin, V. P.; Lab, M. J.; Moss, G. W. J.; Frolenkov, G. I.; Klenerman, D.; Korchev, Y. E. *Nat. Methods* **2009**, *6*, 279–281.
(4) Shevchuk, A. I.; Frolenkov, G. I.; Sanchez, D.; James, P. S.; Freedman, N.; Lab, M. J.; Jones, R.; Klenerman, D.; Korchev, Y. E. *Angew. Chem., Int. Ed.* **2006**, *45*, 2212–2216.
(5) Bocker, M.; Muschter, S.; Schmitt, E. K.; Steinem, C.; Schaffer, T. E. *Langmuir* **2009**, *25*, 3022–3028.
(6) Chen, C. C.; Derylo, M. A.; Baker, L. A. *Anal. Chem.* **2009**, *81*, 4742–4751.
(7) Sanchez, D.; Johnson, N.; Li, C.; Novak, P.; Rheinlaender, J.; Zhang, Y. J.; Anand, U.; Anand, P.; Gorelik, J.; Frolenkov, G. I.; Benham, C.; Lab, M.; Ostanin, V. P.; Schaffer, T. E.; Klenerman, D.; Korchev, Y. E. *Biophys. J.* **2008**, *95*, 3017–3027.
(8) Shevchuk, A. I.; Gorelik, J.; Harding, S. E.; Lab, M. J.; Klenerman, D.; Korchev, Y. E. *Biophys. J.* **2001**, *81*, 1759–1764.
(9) Korchev, Y. E.; Raval, M.; Lab, M. J.; Gorelik, J.; Edwards, C. R. W.; Rayment, T.; Klenerman, D. *Biophys. J.* **2000**, *78*, 2675–2679.
(10) Rothery, A. M.; Gorelik, J.; Bruckbauer, A.; Yu, W.; Korchev, Y. E.; Klenerman, D. *J. Microsc. (Oxford)* **2003**, *209*, 94–101.
(11) Gorelik, J.; Gu, Y. C.; Spohr, H. A.; Shevchuk, A. I.; Lab, M. J.; Harding, S. E.; Edwards, C. R. W.; Whitaker, M.; Moss, G. W. J.; Benton, D. C. H.; Sanchez, D.; Darszon, A.; Vodyanoy, I.; Klenerman, D.; Korchev, Y. E. *Biophys. J.* **2002**, *83*, 3296–3303.
(12) Holt, K. B.; Bard, A. J.; Show, Y.; Swain, G. M. *J. Phys. Chem. B* **2004**, *108*, 15117–15127.
(13) Yamada, H.; Ogata, M.; Koike, T. *Langmuir* **2006**, *22*, 7923–7927.
(14) Wang, H. S.; Li, T. H.; Jia, W. L.; Xu, H. Y. *Biosens. Bioelectron.* **2006**, *22*, 664–669.
(15) Uitto, O. D.; White, H. S. *Anal. Chem.* **2001**, *73*, 533–539.
(16) Kueng, A.; Kranz, C.; Mizaikoff, B. *Biosens. Bioelectron.* **2005**, *21*, 346–353.
(17) Wilburn, J. P.; Wright, D. W.; Cliffel, D. E. *Analyst* **2006**, *131*, 311–316.
(18) Baltes, N.; Heinze, J. *ChemPhysChem* **2009**, *10*, 174–179.
(19) Bard, A. J.; Li, X.; Zhan, W. *Biosens. Bioelectron.* **2006**, *22*, 461–472.
(20) Bauermann, L. P.; Schuhmann, W.; Schulte, A. *Phys. Chem. Chem. Phys.* **2004**, *6*, 4003–4008.
(21) Adams, K. L.; Puchades, M.; Ewing, A. G. *Annu. Rev. Anal. Chem.* **2008**, *1*, 329–355.

imaging by developing and demonstrating a nanopipet probe with an integrated ultramicroelectrode (UME) for concurrent SICM and SECM imaging.

SICM is a scanning probe technique utilizing the ion current through a nanopipet tip as the feedback signal. The ion current feedback signal is generated by applying a bias between an electrode inside the electrolyte-filled nanopipet and an electrode in the surrounding bath solution. As the nanopipet moves close to a surface (within a few tip radii) the flow of ionic species through the tip is hindered and the ion current is reduced. The sensitivity of the ion current to tip−sample spacing facilitates an ion current-based feedback loop to maintain constant tip−sample spacing and enables topographic imaging as the nanopipet is raster-scanned over a surface. This basic feedback loop has been improved upon with the development of distance-modulated feedback protocols,[8,22] which utilize a vertically oscillating nanopipet. As the oscillating nanopipet approaches a surface, its movement generates an alternating current (ac) ion current component at the oscillation frequency that serves as the feedback signal.

SECM[23,24] is another scanning probe technique that instead utilizes a UME probe. SECM imaging relies on a redox mediator in solution to generate a redox current at the UME probe, with the current recorded as a function of position as the probe is raster-scanned over the sample surface. Within this framework, several SECM imaging schemes have been developed, including feedback-mode[25,26] and substrate generation/tip collection (SG/TC)-mode imaging.[27,28] Feedback-mode imaging exploits the variation in the redox current as the UME approaches a surface, with the sign of this variation depending upon the conductivity of the surface. At a conducting surface, redox species are regenerated at the surface, resulting in an increased redox current known as positive feedback. Conversely, at an insulating surface, the diffusion of redox species to the UME is hindered, resulting in reduced redox current known as negative feedback. Alternatively, SG/TC imaging detects redox species generated at the sample surface. This imaging mode requires independent biasing of the UME and sample, with the sample biased to generate (oxidize or reduce) species in solution and the UME biased to collect (reduce or oxidize) the species generated at the sample.

Despite its many applications, SECM suffers from a number of limitations. Successful SECM imaging requires maintaining a tip−sample spacing of a few electrode radii. However, feedback-controlled probe positioning is complicated by differing feedback responses over conducting and insulating surfaces. As a result, SECM is most commonly conducted in constant-height mode, resulting in the convolution of sample topography and electro-chemical activity, which complicates the interpretation of observed redox current variations. The difficulty in maintaining the requisite

tip−sample spacing also limits the spatial resolution of SECM imaging, since high spatial resolution requires small-diameter UMEs and correspondingly small tip−sample spacings.[29]

The limitations of SECM are most commonly addressed by adopting constant-distance mode imaging schemes, in which the tip−sample spacing is maintained independently of the redox current. A number of strategies for constant-distance SECM have been demonstrated, including alternating current SECM (ac-SECM),[30,31] shear-force distance control SECM,[32] and scanning electrochemical microscopy−atomic force microscopy (SECM−AFM).[33−36] The integrated SECM−SICM strategy implemented in this paper is an alternative route to constant-distance imaging that provides the advantages of noncontact SICM imaging and tip-position-modulated SECM (TPM-SECM).[37,38] TPM-SECM is analogous to distance-modulated SICM, utilizing a vertically oscillated UME and a lock-in amplifier to detect the ac component of the redox current in close proximity to a surface. In comparison to conventional SECM, TPM-SECM possesses improved signal-to-noise ratio and eliminates the direct current (dc) offset from the SECM current signal.

Integrated SECM−SICM imaging requires a suitable nanopipet probe, with a small-diameter tip for SICM imaging and an integrated UME for SECM imaging. A number of pipet-based probes have previously been demonstrated for SECM imaging. Walsh et al. demonstrated a 3 μm diameter micropipet by insulating gold-coated micropipets with electrophoretic paint.[39] However, these probes are relatively large for SICM imaging, and electrophoretic paint insulation requires significant precautions to prevent clogging of the tip. More recently, Williams et al. demonstrated the scanning micropipet contact method (SMCM),[40] utilizing a micropipet for high-resolution electrochemical imaging. Despite its attributes, SMCM does not provide concurrent topographic imaging nor does it correlate topographic and electrochemical features.

A suitable SECM−SICM probe requires a completely insulated gold-coated nanopipet with the gold film exposed as a UME in immediate proximity to the nanopipet tip. Multiple insulation schemes have previously been reported for UME fabrication, including dipping into molten Apiezon wax[41] and electrophoretic paint methods.[42,43] However, these approaches are not well-suited to nanopipet insulation, as they may occlude the nanopipet tip.

(22) Pastre, D.; Iwamoto, H.; Liu, J.; Szabo, G.; Shao, Z. F. *Ultramicroscopy* **2001**, *90*, 13−19.
(23) Bard, A. J.; Fan, F. R. F.; Kwak, J.; Lev, O. *Anal. Chem.* **1989**, *61*, 132−138.
(24) Bard, A. J., Mirkin, M. V., Eds. *Scanning Electrochemical Microscopy*; Marcel Dekker: New York, 2001.
(25) Kwak, J.; Bard, A. J. *Anal. Chem.* **1989**, *61*, 1221−1227.
(26) Kwak, J.; Bard, A. J. *Anal. Chem.* **1989**, *61*, 1794−1799.
(27) Engstrom, R. C.; Weber, M.; Wunder, D. J.; Burgess, R.; Winquist, S. *Anal. Chem.* **1986**, *58*, 844−848.
(28) Engstrom, R. C.; Wightman, R. M.; Kristensen, E. W. *Anal. Chem.* **1988**, *60*, 652−656.

(29) Shao, Y. H.; Mirkin, M. V.; Fish, G.; Kokotov, S.; Palanker, D.; Lewis, A. *Anal. Chem.* **1997**, *69*, 1627−1634.
(30) Alpuche-Aviles, M. A.; Wipf, D. O. *Anal. Chem.* **2001**, *73*, 4873−4881.
(31) Ervin, E. N.; White, H. S.; Baker, L. A. *Anal. Chem.* **2005**, *77*, 5564−5569.
(32) Hengstenberg, A.; Kranz, C.; Schuhmann, W. *Chem.−Eur. J.* **2000**, *6*, 1547−1554.
(33) Macpherson, J. V.; Unwin, P. R. *Anal. Chem.* **2000**, *72*, 276−285.
(34) Kranz, C.; Friedbacher, G.; Mizaikoff, B. *Anal. Chem.* **2001**, *73*, 2491−2500.
(35) Burt, D. P.; Wilson, N. R.; Weaver, J. M. R.; Dobson, P. S.; Macpherson, J. V. *Nano Lett.* **2005**, *5*, 639−643.
(36) Davoodi, A.; Farzadi, A.; Pan, J.; Leygraf, C.; Zhu, Y. *J. Electrochem. Soc.* **2008**, *155*, C474−C485.
(37) Wipf, D. O.; Bard, A. J. *Anal. Chem.* **1992**, *64*, 1362−1367.
(38) Wipf, D. O.; Bard, A. J.; Tallman, D. E. *Anal. Chem.* **1993**, *65*, 1373−1377.
(39) Walsh, D. A.; Fernandez, J. L.; Mauzeroll, J.; Bard, A. J. *Anal. Chem.* **2005**, *77*, 5182−5188.
(40) Williams, C. G.; Edwards, M. A.; Colley, A. L.; Macpherson, J. V.; Unwin, P. R. *Anal. Chem.* **2009**, *81*, 2486−2495.
(41) Nagahara, L. A.; Thundat, T.; Lindsay, S. M. *Rev. Sci. Instrum.* **1989**, *60*, 3128−3130.
(42) Schulte, A.; Chow, R. H. *Anal. Chem.* **1996**, *68*, 3054−3058.
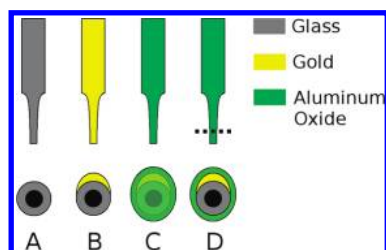
Figure 1. Schematic of integrated SECM−SICM nanopipet probe fabrication viewed normal to and along the nanopipet axis: (A) as-pulled borosilicate nanopipet, (B) deposited gold electrode film with titanium adhesion layer, (C) ALD Al_2O_3 insulating film, and (D) FIB milling to expose the UME and open the nanopipet tip.

To circumvent these issues, we utilize atomic layer deposition (ALD) of aluminum oxide (Al_2O_3) for the insulating film. ALD is optimally suited for the high-quality insulation of an irregularly shaped structure, such as a nanopipet, due to its excellent conformality and thickness control.[44] Additionally, ALD is a parallel process that provides simultaneous and reproducible insulation of arrays of probes. Following insulation by ALD, we utilize focused ion beam (FIB) milling to expose the gold film as a UME, since FIB milling is an established and compatible means for preparing UMEs of precise dimensions.[34,45]

Herein, we describe both the fabrication and application of integrated SECM−SICM probes. The fabricated probes are characterized by scanning electron microscopy (SEM) to image probe morphology and cyclic voltammetry (CV) to assess electrochemical response. The suitability of the probes for SECM−SICM is demonstrated via approach curves to both conducting and insulating surfaces. Lastly, feedback-mode and SG/TC-mode SECM−SICM imaging are accomplished on patterned surfaces with lateral dimensions as small as 180 nm.

EXPERIMENTAL SECTION

Solutions and Materials. All solutions were prepared with 18 MΩ·cm deionized water. Redox mediators of hexaammineruthenium(III) chloride ($Ru(NH_3)_6Cl_3$, 98%), potassium ferricyanide(III) ($K_3Fe(CN)_6$, 99%), and ferrocenemethanol (97%) and supporting electrolytes of potassium chloride (KCl) and potassium nitrate (KNO_3) were acquired from Sigma-Aldrich (St. Louis, MO).

SECM−SICM Probe Fabrication. The SECM−SICM probe fabrication procedure is shown in Figure 1. Nanopipets were pulled from borosilicate glass capillaries (1 mm o.d., 0.5 mm i.d. with filament, Sutter Instruments, Novato, CA) with a CO_2 laser-based pipet puller (P-2000, Sutter Instruments). Through experimentation with puller recipes, the as-pulled nanopipet tips were consistently 200 nm in diameter with a 100 nm diameter opening, as measured by SEM. A 200−250 nm gold electrode film with a 5 nm titanium adhesion layer was electron beam evaporated onto one side of the nanopipets. The gold-coated nanopipets were then insulated by 70−100 nm of Al_2O_3
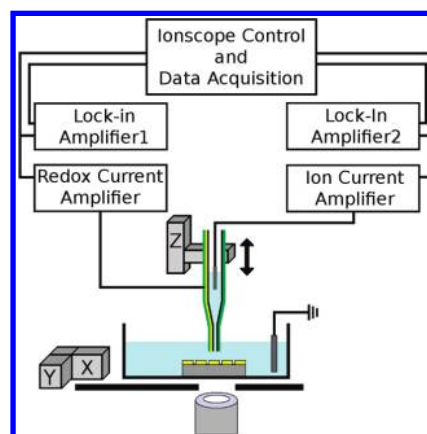
Figure 2. Schematic of the SECM−SICM imaging instrumentation.

deposited by ALD in a viscous flow type reactor.[46,47] After loading into the reactor, the nanopipets were cleaned by flowing ozone to remove any adventitious carbon. Al_2O_3 films were deposited at a temperature of 200 °C with trimethylaluminum and water reactants iteratively pulsed into the reactor with nitrogen carrier gas at dose times of 1 s and purge times of 5 s. The Al_2O_3 deposition rate was approximately 0.105 nm/cycle. The insulated nanopipets were FIB-milled to expose the gold film as a UME and ensure an open nanopipet tip. FIB milling was conducted in a dual-beam FIB tool (FEI Helios Nanolab, Hillsboro, OR) with a 30 kV, 0.28 pA ion beam. Nanopipets were mounted gold side down onto the FIB stage with conductive copper tape to ensure electrical contact to the nanopipet and minimize charging during imaging and milling. Milling was conducted normal to the nanopipet axis in a multistep process. The nanopipet was first milled to an outer diameter of ∼800 nm. SEM imaging was then used to confirm that the UME was exposed and that the nanopipet tip was open. After confirmation, a final single pass milling step was used to clean the exposed UME surface.

Instrumentation. A schematic of the SECM−SICM instrumentation is shown in Figure 2. SICM imaging was achieved with a commercially available SICM instrument (ScanIC, ionscope, London, U.K.). The nanopipet was mounted onto a single-axis piezo scanner for oscillation and feedback-controlled movement in the z direction. Samples were placed into a small Petri dish filled with solution. The Petri dish rests on a separate piezo scanner that rasters in the x and y directions for SICM imaging. The entire SICM microscope rests above an inverted optical microscope stage for positioning of the pipet relative to the sample.

Conventional SICM imaging utilizes two electrodes. A Ag/AgCl electrode in the bath solution was grounded and served as the reference electrode for all applied potentials, and a separate Ag/AgCl electrode was placed inside the nanopipet and biased to generate an ion current through the tip. The ion current was amplified, with the ac component of the ion current serving as the feedback signal for SICM topographic imaging. For integrated SECM−SICM imaging, a third electrode connection was made

(43) Slevin, C. J.; Gray, N. J.; Macpherson, J. V.; Webb, M. A.; Unwin, P. R. *Electrochem. Commun.* **1999**, *1*, 282–288.

(44) Hoivik, N. D.; Elam, J. W.; Linderman, R. J.; Bright, V. M.; George, S. M.; Lee, Y. C. *Sens. Actuators, A* **2002**, *103*, 100–108.

(45) Qiao, Y.; Chen, J.; Guo, X. L.; Cantrell, D.; Ruoff, R.; Troy, J. *Nanotechnology* **2005**, *16*, 1598–1602.

(46) Groner, M. D.; Fabreguette, F. H.; Elam, J. W.; George, S. M. *Chem. Mater.* **2004**, *16*, 639–645.

(47) Elam, J. W.; Groner, M. D.; George, S. M. *Rev. Sci. Instrum.* **2002**, *73*, 2981–2987.

to the integrated UME, and the redox current was amplified by a low-noise patch-clamp amplifier (AxoPatch 200B, Molecular Devices, Sunnyvale, CA). The ac ion and redox current signals were measured using two separate lock-in amplifiers (SR850, Stanford Research Systems, Sunnyvale, CA), with the drive voltage for nanopipet oscillation serving as the reference signal. For each ac current signal, the phase shift between the reference signal and the current signal was first zeroed with the probe in close proximity to a gold surface. The in-phase component of the ac signal was then recorded for all ac measurements. Lastly, a low-noise digitizer (Digidata 1440A, Molecular Devices) was used to apply all electrode potentials and to monitor and record all signals.

SECM–SICM Probe Characterization. The fabricated probes were filled with a solution of 100 mM KNO_3 and 0.1% w/v Triton X-100 surfactant, mounted into the SICM, and lowered into the bath solution for characterization. Cyclic voltammograms were acquired in 4.7 mM ferrocenemethanol, 100 mM KNO_3 solution to assess the electrochemical behavior of the UME. A two-electrode geometry, with the UME as the working electrode and the Ag/AgCl bath electrode as the counter electrode, was utilized. The potential was swept from −200 to 600 mV versus Ag/AgCl at 20 mV/s.

Approach curves were acquired in 10 mM $Ru(NH_3)_6Cl_3$, 100 mM KNO_3 solution with the ion and redox currents recorded as the nanopipet approaches a surface. The UME was biased at −500 mV versus Ag/AgCl to ensure $Ru(NH_3)_6^{3+}$ reduction. The nanopipet electrode voltage was set to generate a suitable ion current for SICM feedback and did not significantly impact the redox current signal (see the Supporting Information). The probe position was controlled using SICM feedback. As the SICM feedback setpoint was varied to move the probe closer to and further from the surface, the dc and ac components of the ion and redox currents were recorded. Approach curves were acquired in this manner over both conducting gold surfaces and insulating Teflon surfaces.

SECM–SICM Imaging. Feedback-mode and SG/TC-mode SECM–SICM images were acquired to demonstrate the imaging characteristics of the nanopipet probes. In both cases, the SICM topography imaging was conducted in ac mode, with the nanopipet oscillated at an amplitude of 50 nm_{rms} and a frequency of 570 Hz. At these small oscillation amplitudes relative to the UME dimensions, we do not expect the oscillation to significantly impact the electrochemical response of the integrated UME. Feedback-mode images of FIB-patterned test structures were acquired in 10 mM $Ru(NH_3)_6Cl_3$, 100 mM KNO_3 solution. The test structures consisted of arrays of narrow trenches with variable widths and spacings milled into a 30 nm gold film with a 5 nm titanium adhesion layer on a glass substrate, resulting in narrow insulating trenches of exposed glass separated by broader conducting regions of gold. For imaging, the nanopipet electrode was biased to generate a suitable ion current and the UME was biased at −500 mV versus Ag/AgCl for $Ru(NH_3)_6^{3+}$ reduction. Topography, dc redox current, and ac redox current images were concurrently acquired by the SICM control software.

SG/TC-mode images were acquired in a 10 mM $K_3Fe(CN)_6$, 100 mM KCl solution. Samples consisted of 30 nm thick, 10 μm wide gold electrodes defined by photolithography and lift-
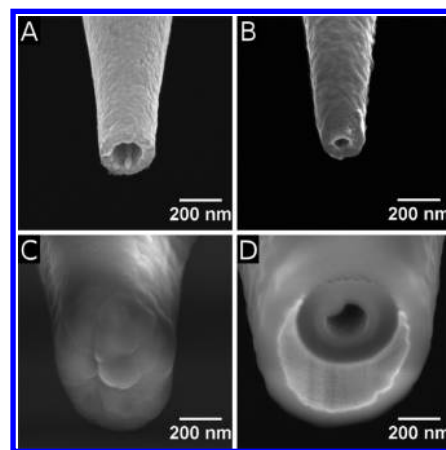
Figure 3. SEM images of the SECM–SICM nanopipet throughout the fabrication process: (A) as-pulled borosilicate nanopipet with 30 nm AuPd film to minimize charging, (B) after evaporation of the gold electrode film with titanium adhesion layer, (C) after ALD of 100 nm thick Al_2O_3 with occluded nanopipet tip, and (D) after FIB milling to expose the gold and open the nanopipet tip.

off on a thermally oxidized silicon substrate. For imaging, the sample was biased at −200 mV to ensure reduction of $Fe(CN)_6^{3-}$ and the UME was biased at 600 mV for oxidation of the $Fe(CN)_6^{4-}$ generated at the sample. Topography and dc redox current were concurrently acquired by the SICM control software.

RESULTS AND DISCUSSION

Pipet Fabrication. SEM images of the SECM–SICM probe at the various stages of fabrication are shown in Figure 3. The relevant dimensions are the inner diameter of the nanopipet tip and the dimensions of the UME. The inner diameter of the nanopipet tip dictates both the lateral and vertical resolution for topographic imaging, so it is desirable to minimize this dimension.[48] The fabricated probe has an inner diameter of approximately 100 nm, which is consistent with nanopipet diameters commonly used for SICM imaging. Similarly, the electrochemical spatial resolution of the probe is dictated by the UME dimensions, with a spatially localized UME necessary for high-resolution imaging. To minimize the spatial dimensions of the UME, the gold electrode film was evaporated onto only one side of the pipet. As a result, the UME is crescent-shaped with a thickness of approximately 220 nm and a maximum dimension equal to the pipet outer diameter of 500 nm.

The deposition of a continuous, high-quality insulating film is critical to defining the UME solely at the tip. As shown in Figure 3D, the ALD Al_2O_3 is highly conformal and coats both the inner and outer surfaces of the nanopipet. Although the conformal coating of the outer surface is critical for insulating the gold film, the conformal coating of the inner surface introduces a number of issues that have been overcome. First, the Al_2O_3 film completely occludes the tip. The extent of this occlusion depends upon the thickness of the Al_2O_3 film, as deposition inside the nanopipet continues through its larger end even after the tip has been occluded. This results in a trade-off between insulating film thickness and overall probe dimensions, as thicker insulating films require FIB milling further up the

(48) Rheinlaender, J.; Schaffer, T. E. *J. Appl. Phys.* **2009**, *105*, 094905.
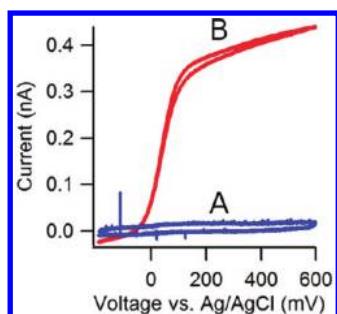
Figure 4. Cyclic voltammograms acquired in 4.7 mM ferrocenemethanol, 100 mM KNO_3 solution: (A) before FIB milling and (B) after FIB milling to expose the integrated nanopipet UME.

nanopipet shank in order to obtain an open tip. Second, the conformal Al_2O_3 adversely affects nanopipet filling. SICM requires a continuous electrolyte path to the tip. For this reason, we commonly use filamented pipets, which contain a small glass filament inside the pipet to reduce surface tension and ease filling. However, after Al_2O_3 deposition, complete filling with electrolyte solution is rarely achieved. To reliably fill the nanopipet after Al_2O_3 deposition, it is necessary to add 0.1% w/v Triton X-100 to the filling solution.

Electrochemical Characterization. Cyclic voltammograms reveal the effectiveness of both the Al_2O_3 insulating film and the FIB UME exposure. Voltammograms were acquired in 4.7 mM ferrocenemethanol, 100 mM KNO_3 solution. As shown in Figure 4, the Al_2O_3-insulated probe exhibits no redox current prior to FIB milling, indicating a continuous, pinhole-free insulating film. We have found that a minimum Al_2O_3 thickness of 70 nm is necessary to achieve complete insulation. After FIB milling, the characteristic UME sigmoidal response is observed with a steady-state current of 360 pA, indicating successful electrode exposure.

Well-defined relationships between steady-state current and electrode dimensions do not exist for crescent-shaped UMEs, as they do for more conventional geometries.[49] As a result, the relationship for an inlaid disk microelectrode is used as an approximation. The steady-state current at an inlaid disk microelectrode is given by the expression

$$i_{ss} = 4nFDCr$$

where n is number of electrons transferred, F is Faraday's constant, D is diffusion coefficient, C is concentration, and r is UME radius. On the basis of the observed steady-state current, the effective radius of the UME is calculated to be 294 nm. For comparison, an alternative effective radius was calculated based on the total exposed area of the UME observed in SEM. With this approach, the effective radius was calculated to be 245 nm, which compares well with the cyclic voltammetry measurement.

Approach Curves. Approach curves confirm both the feedback response of the integrated UME as it approaches a surface and the independence of the ion and redox current signals. Figures 5 and 6 show the variations in the dc and ac components of the ion and redox currents on approach to a conducting gold surface and an insulating Teflon surface, respectively. In both

(49) Zoski, C. G. *Electroanalysis* **2002**, *14*, 1041–1051.
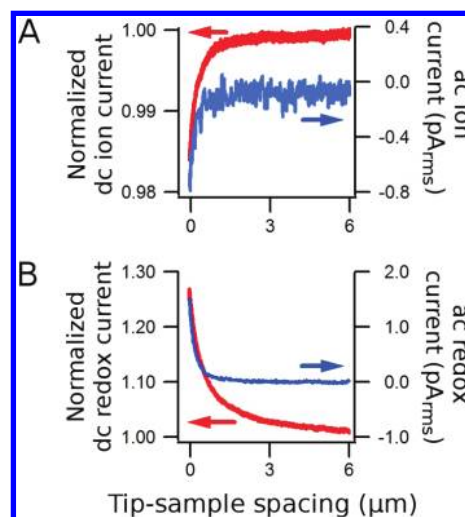
Figure 5. Approach curves to a conducting gold surface collected in 10 mM $Ru(NH_3)_6Cl_3$, 100 mM KNO_3 solution: (A) normalized dc ion current and ac ion current response; (B) normalized dc redox current and ac redox current response.
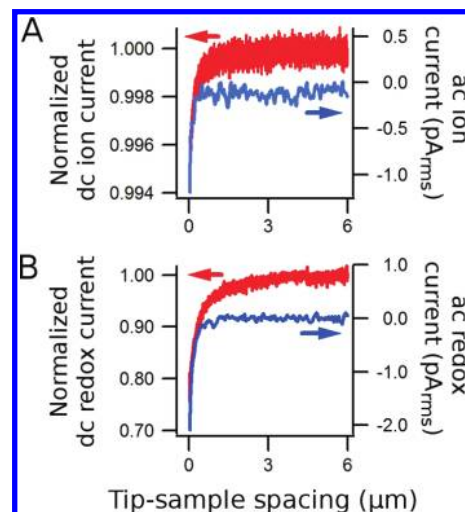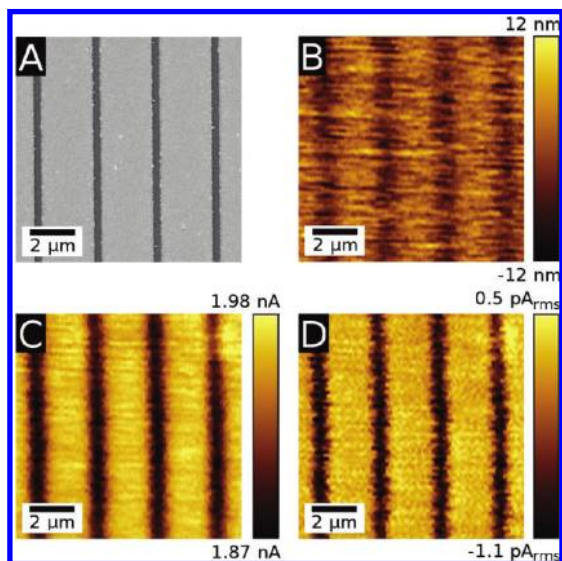

Figure 6. Approach curves to an insulating Teflon surface collected in 10 mM $Ru(NH_3)_6Cl_3$, 100 mM KNO_3 solution: (A) normalized dc ion current and ac ion current response; (B) normalized dc redox current and ac redox current response.

cases, the dc currents are normalized with respect to their values measured far from the surface.

The dc ion current exhibits similar behavior on approach to either surface. This observation is consistent with the SICM feedback mechanism, which depends solely on the hindered diffusion of ionic species to the nanopipet tip and is substrate independent. The ac ion current is also consistent with expectations, with an increased ac component upon approach. At large tip−sample distances, the ion current is unperturbed by the relatively small oscillation amplitude of the probe. However, as the probe approaches the surface and the oscillation amplitude becomes significant relative to the tip−sample spacing, this ac component increases in magnitude.

On the other hand, the redox current exhibits substrate-dependent behavior on approach to conducting and insulating surfaces, consistent with the SECM feedback mechanism. As the integrated UME approaches a conducting gold surface, the dc current increases due to recycling of the UME-generated species.
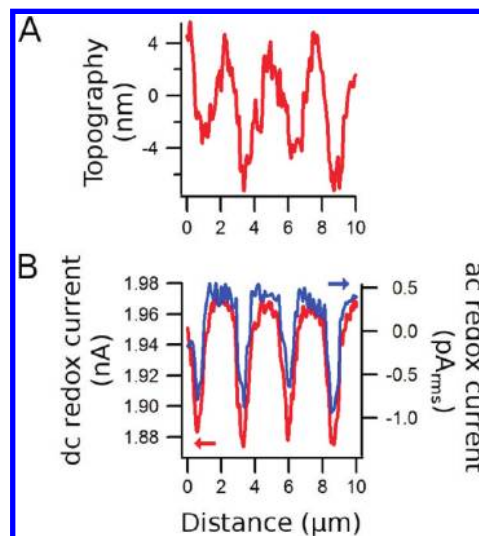
Figure 7. SEM and feedback-mode SECM−SICM images of 400 nm wide trenches FIB-milled into a gold film on a glass substrate; SECM−SICM images were acquired in 10 mM Ru(NH$_3$)$_6$Cl$_3$, 100 mM KNO$_3$ solution: (A) SEM, (B) SECM−SICM topography, (C) SECM−SICM dc redox current, and (D) SECM−SICM ac redox current.

Conversely, as the probe approaches an insulating Teflon surface, the dc current decreases due to hindered diffusion at the UME. Similarly, the ac current also depends upon surface conductivity. Like the ion current, the redox current has no ac component at large tip−sample spacings and increases on approach to the surface. However, the ac redox current responses to conducting and insulating surfaces are 180° out of phase. This phase shift can be explained by approximating the ac response as the derivative of the dc response. Positive feedback over conducting surfaces results in increased dc current and positive ac response, whereas negative feedback over insulating surfaces results in decreased dc current and negative ac response.

The ac redox current has significant advantages over the dc redox current as an electrochemical imaging signal. As shown in Figures 5 and 6, the ac signal is more surface-sensitive than the dc signal, with variations occurring at smaller tip−sample spacings relative to the dc signal. Furthermore, the ac signal eliminates the large dc offset current associated with the steady-state response of the UME, making small variations in the ac current easier to detect than small variations in the dc current.[37] This effect has implications for the probe fabrication as well. With dc current, any defects in the probe's insulating film produce an increased dc offset current, which complicates small signal detection. However, the ac current will remain insensitive to many of these defects, as defects far from the tip will be too far from the surface to generate an ac response. This reduced sensitivity to defects is useful, as the deposition of a high-quality, pinhole-free insulating film is one of the primary challenges in fabricating SECM probes.

Integrated SECM−SICM Imaging. Integrated SECM−SICM imaging is demonstrated by both feedback-mode and SG/TC-mode imaging on patterned substrates. Feedback-mode imaging was conducted on FIB-milled test structures in a solution of 10 mM Ru(NH$_3$)$_6$Cl$_3$, 100 mM KNO$_3$. Figure 7 shows SEM images of the fabricated test structure and corresponding SECM−SICM topography, dc redox current, and ac redox current images. As


Figure 8. Line profiles from feedback-mode SECM−SICM imaging of 400 nm wide FIB-milled, glass-exposed trenches: (A) topography and (B) dc and ac redox current.

shown in Figure 7A, the test structure consists of 400 nm wide trenches with a center-to-center spacing of 2.625 μm that were FIB-milled into a gold film to expose the underlying glass substrate. These recessed features are narrower than the overall diameter of the fabricated SECM−SICM probe, preventing the full extension of the probe into the trench; yet the trenches are still detected in the SICM topography image, indicating successful surface tracking via SICM feedback and allowing comparison between the topographic and electrochemical features.

Correlation of the topography and redox current images reveals the expected contrast in both the dc and ac redox current images, with enhanced redox current over the broad gold regions, consistent with positive feedback, and reduced redox current over the narrow insulating trenches, consistent with negative feedback. As shown in the line profile in Figure 8, the redox current signals exhibit some convolution between the trench and UME dimensions, resulting in an observed full width at half-maximum (fwhm) of 680 nm in the dc redox current and 580 nm in the ac redox current. Despite this lateral broadening, the UME is still capable of resolving the trenches as isolated features, with the redox current returning to a near-constant value between trenches. Additionally, the reduced fwhm of the ac redox current indicates a slight enhancement in lateral resolution of the ac redox current compared to the dc redox current. Lastly, the line profiles also reveal a lateral offset of 230 nm between the topographic and redox current signals. This lateral offset is due to the asymmetry of the probe, with the UME being on only one side of the nanopipet, and is consistent with the center-to-center spacing of the nanopipet tip and the integrated UME. These images demonstrate the maximum offset condition; however, as these dimensions are known, they can be readily anticipated and compensated for during imaging.

As shown in Figure 9, SECM−SICM images were also acquired of 180 nm wide trenches separated by 875 nm to further characterize the spatial resolution of the probes. At these reduced dimensions, the probes are still capable of detecting the trenches in SICM topography, dc redox current, and ac redox current images. However, the smaller trenches are more difficult to detect
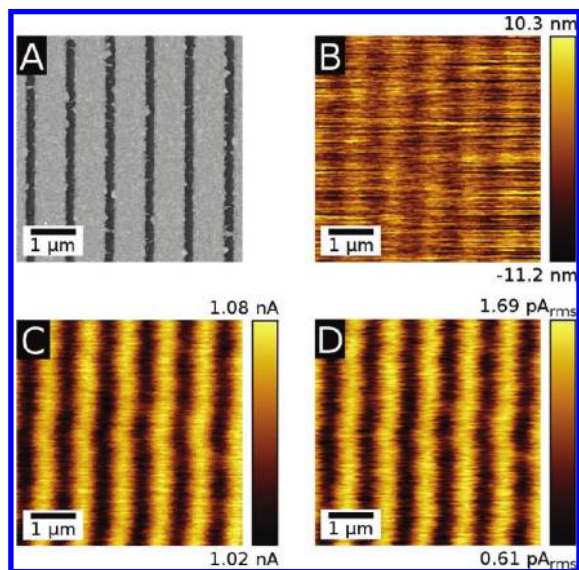
Figure 9. SEM and feedback-mode SECM−SICM images of 180 nm wide trenches FIB-milled into a gold film on a glass substrate; SECM−SICM images were acquired in 10 mM $Ru(NH_3)_6^{3+}$, 100 mM KNO_3: (A) SEM, (B) SECM−SICM topography, (C) SECM−SICM dc redox current, and (D) SECM−SICM ac redox current.
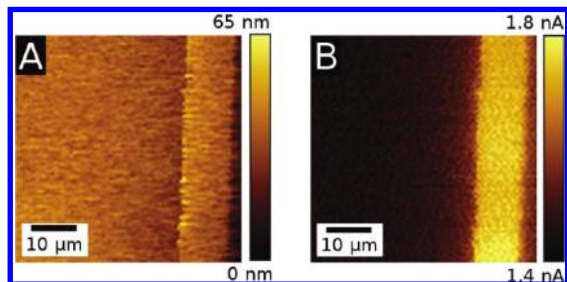
Figure 10. SG/TC-mode SECM−SICM images of 10 μm wide gold electrode acquired in 10 mM $K_3Fe(CN)_6$, 100 mM KCl solution: (A) topography and (B) dc redox current.

in topographic imaging, and the lateral broadening of the redox current signals is more significant relative to the intertrench spacing. Despite these convolution effects, the trenches are still resolved as isolated features, which demonstrates that the probes are capable of detecting features in the deep submicrometer regime.

The application of the SECM−SICM probes for SG/TC-mode imaging was demonstrated on a 30 nm thick, 10 μm wide gold electrode in a solution of 10 mM $K_3Fe(CN)_6$, 100 mM KCl. In particular, Figure 10 shows SECM−SICM images of the sample topography and dc redox current. The 10 μm wide electrode is clearly visible in the SICM topography image. Correlation of the topography and redox current images show enhanced collection

(oxidation) current over the gold electrode, indicating the localized generation and collection of redox species over the gold electrode. Additionally, there is relatively little broadening in the redox current image, indicating a small, localized integrated UME on the nanopipet probe.

CONCLUSION

In this work, we have demonstrated the successful fabrication and application of integrated SECM−SICM nanopipet probes. Integrated SECM−SICM probe fabrication utilizes ALD and FIB milling, with ALD providing highly conformal and reproducible insulation of many nanopipet probes at a time and FIB milling providing controlled exposure of a UME at the nanopipet tip. Cyclic voltammetry reveals that this fabrication procedure yields an integrated UME with an effective radius of 294 nm, which is consistent with SEM characterization of the probe. Approach curves on conducting and insulating substrates demonstrate the suitability of these probes for SICM and SECM with the ac redox current showing enhanced surface sensitivity. Integrated SECM−SICM imaging in both feedback- and SG/TC-mode imaging is demonstrated with spatial resolution in the deep submicrometer regime. This work extends the capabilities of conventional SICM imaging to the characterization of electrochemical phenomena, thus enabling new opportunities for biological and electrochemical imaging.

SUPPORTING INFORMATION AVAILABLE

Ion and redox current responses as a function of the nanopipet electrode voltage, and redox current approach curves to insulating surfaces, demonstrating the independence of the feedback response from the nanopipet electrode voltage. This material is available free of charge via the Internet at http://pubs.acs.org.